Materials Science & Engineering C 121 (2021) 111733

Contents lists available at ScienceDirect

Materials Science & Engineering C

journal homepage: www.elsevier.com/locate/msec

Short communication

Tailoring biocompatible Ti-Zr-Nb-Hf-Si metallic glasses based on high-entropy alloys design approach

Mariana Calin [a,*], Jithin Vishnu [b], Pramote Thirathipviwat [a], Monica-Mihaela Popa [a], Maria Krautz [a], Geetha Manivasagam [b], Annett Gebert [a]

[a] Institute for Complex Materials, Leibniz Institute for Solid State and Materials Research, Dresden (IFW Dresden), Helmholtzstr-20, D-01069 Dresden, Germany
[b] Centre for Biomaterials Cellular and Molecular Theranostics, CBCMT, Vellore Institute of Technology, Vellore, India

ARTICLE INFO

Keywords:
Metallic glass
Biomaterial
High entropy alloy
Corrosion
Magnetic properties
Radiopacity

ABSTRACT

Present work unveils novel magnetic resonance imaging (MRI) compatible glassy Ti-Zr-Nb-Hf-Si alloys designed based on a high entropy alloys approach, by exploring the central region of multi-component alloy phase space. Phase analysis has revealed the amorphous structure of developed alloys, with a higher thermal stability than the conventional metallic glasses. The alloys exhibit excellent corrosion properties in simulated body fluid. Most importantly, the weak paramagnetic nature (ultralow magnetic susceptibility) and superior radiopacity (high X-ray attenuation coefficients) offer compatibility with medical diagnostic imaging systems thereby opening unexplored realms for biomedical applications.

1. Introduction

Increased incidence of occlusive vascular diseases associated with aneurysms and coronary/peripheral artery diseases demand the usage of small and complex shaped devices such as aneurysm clips and stents [1–3]. For these medical applications a critical follow-up inspection with the aid of magnetic resonance imaging (MRI) is inevitable. However, this post-operative diagnosis with non-invasive MRI technique is often hindered by magnetic artefact generation by the high magnetic susceptibility of the implant material. It is highly imperative to develop novel materials with lower magnetic susceptibility accompanying adequate mechanical properties, corrosion resistance, biocompatibility and processability at the required level of complexity. In the quest for such MRI-compatible materials several crystalline alloy systems such as Zr-Nb-Sn [4], Nb-28Ta-3.5W-1.3Zr [5], Zr-Ru [6], Zr-4Mo-4Sn [6], Zr-X (X = Hf, Ru, Mo) [7] and Ti-Ta/Ir [8] alloys have been explored.

Metallic glasses (MGs) represent a particular class of amorphous alloys with disordered atomic structure resulting from the suppression of crystallization during solidification [9]. Such exceptional structural state without any microstructural defects can develop ultrahigh strength, large elastic strains, excellent wear and corrosion resistance, net castability and remarkable precise formability that are advantageous for stents as well as aneurysm clips on length scales in micro-/millimetre range [10,11].

In general, bulk metallic glasses (BMGs) have multicomponent compositions selected to optimize their glass-forming ability (GFA), described as the tendency for materials to form glassy phase. The main design concept of BMGs is to select one element as a base (such as Ti, Zr, Fe, Pd, etc.) and some other elements to match the base element for a good GFA. Ti and Zr-based BMGs have been widely investigated as potential biomaterials [10,12]. However, their use is limited because of the incorporation of cytotoxic and allergic elements such as Ni and Cu [13–15], which are good glass-formers. Presence of Ni can elicit allergic and carcinogenic symptoms [16] whereas a high amount of Cu could facilitate the pitting corrosion process [17,18]. Moreover, only very few studies have been carried out so far [19,20] on the magnetic susceptibility and radiopacity of the non-ferromagnetic MGs in relation to biomedical imaging. In an effort to develop novel biocompatible MGs with an appropriate combination of biomedical properties as well as MRI compatibility, in this study we have adopted a new composition design strategy based on the high-entropy alloys approach by exploring the central region of multi-component alloy phase space of the Ti-Zr-Nb-Hf-Si system.

In contrast to conventional alloys, typically composed of only one or two principal elements, the high entropy alloys (HEAs) consist of five or more elements with (near) equiatomic concentration, which form single-phase solid solutions [21]. HEAs field has inspired the exploration of the vast composition space offered by so-called “multi-principal

* Corresponding author.
E-mail address: M.Calin@ifw-dresden.de (M. Calin).

https://doi.org/10.1016/j.msec.2020.111733
Received 30 June 2020; Received in revised form 16 October 2020; Accepted 11 November 2020
Available online 14 November 2020

element alloys" (MPEAs) [22]. Deviation from the single-phase solid solution rule has been reported [21,23,24] suggesting the formation of intermetallic compounds or even amorphous phases. Equiatomic multicomponent bulk amorphous alloys were synthesized for $Ti_{20}Zr_{20}Hf_{20}Cu_{20}(Fe/Ni/Co)_{20}$ [25], $Pd_{20}Pt_{20}Cu_{20}Ni_{20}P_{20}$ [26], $Ti_{20}Zr_{20}Cu_{20}Ni_{20}Be_{20}$ [27] and $Sr_{20}Ca_{20}Yb_{20}Mg_{20}Zn_{20}$ [28]. However, all these metallic glasses contain toxic and/or allergic elements such as Be and Ni, which limit their biomedical applications.

In this contribution, we report for the first time the formation of multi-principal element alloys (MPEAs) with amorphous structure and no harmful alloying additions, namely $Ti_{20}Zr_{20}Nb_{20}Hf_{20}Si_{20}$, $Ti_{30}Zr_{25}Nb_{25}Si_{15}Ga_3B_2$ and $Ti_{20}Zr_{20}Nb_{20}Hf_{20}Si_{15}Ga_3B_2$. GFA, thermal stability, corrosion behaviour, magnetic and radiopacity properties have been investigated. We show that the HEA approach is another effective route for designing biocompatible metallic glasses with appropriate properties for small medical implants.

2. Experimental details

Alloy ingots with nominal compositions (in at.%), $Ti_{25}Zr_{25}Nb_{25}Hf_{25}$, $Ti_{20}Zr_{20}Nb_{20}Hf_{20}Si_{20}$, $Ti_{30}Zr_{25}Nb_{25}Si_{15}Ga_3B_2$ and $Ti_{20}Zr_{20}Nb_{20}Hf_{20}Si_{15}Ga_3B_2$ (referred to as alloy A0, A1, A2 and A3, respectively) were prepared by arc melting of high purity elements (purity > 99.9%) in a Ti-gettered argon atmosphere. Rapidly solidified ribbons (thickness = ~30 μm, width = ~3 mm) from A1, A2 and A3 were then prepared via a Bühler melt-spinner with a water cooled copper wheel with diameter of 0.20 m. The tangential speed of the copper wheel was of 41 m/s for all the ribbons. The melt temperature was controlled by varying the induction coil power but other melt-spinning processing parameters such as vacuum, pressure, wheel speed and sample dimensions were kept constant for all the alloys. An infrared pyrometer was used to measure the temperature of the melt prior to casting/melt-spinning. The overheating temperature range of the melt during melt-spinning was 1973–2373 K. $Ti_{25}Zr_{25}Nb_{25}Hf_{25}$ (A0) was prepared by injection casting as rods of 3 mm in diameter.

Phase analysis was performed by X-ray diffraction (XRD) using a Philips PANalytical X'Pert PRO diffractometer (Co-$K_{\alpha 1}$ radiation). Thermal stability was studied by Differential Scanning Calorimetry (DSC NETZSCH 404C) at a heating rate of 20 K/min. For evaluation of corrosion properties, electrochemical measurements (using a Solartron SI-1287) were conducted in N_2-purged Ringer's solution with pH 7.4 at 37 °C. Details on the electrochemical measurements are given in Ref. [14]. Field dependent magnetization was measured using a Quantum Design MPMS-XL device with applied fields between −3000 to 3000 kA/m at room temperature. Mass susceptibility was determined as the slope of the linear fit from the recorded M-H curves. Volume susceptibility (unitless) was determined by multiplying the mass susceptibility with density.

3. Results and discussion

Our group has previously developed biocompatible quaternary Ti-Zr-Nb-Si glassy alloys (with Ti > 50 at.%), which exhibited fully amorphous structure, high hardness and strength and excellent corrosion resistance, aiming at exploring the feasibility for bone-related applications [15]. The glass-forming compositions were localized around a deep eutectic from the Ti-rich region of the phase diagram. In the present study we extend the compositional range using a different design approach by exploring the interior regions of hyper-dimensional composition space of the Ti-Zr-Nb-Si-(Hf-Ga-B) with the aim of developing new glassy metallic materials with additional functional properties beneficial for biomedical field, such as imaging after implantation (MRI compatibility and radiopacity).

The starting composition was the $Ti_{25}Zr_{25}Nb_{25}Hf_{25}$ HEA [29], which consists of biocompatible elements with low magnetic susceptibility [30]. Hf brings the advantage of good MRI compatibility (due its lower magnetic susceptibility of about a half of that of Ti and Zr, $\chi_{v,Hf} = 70$ ppm, $\chi_{v,Zr} = 109$ ppm, $\chi_{v,Ti} = 180$ ppm) [30], enhanced radiopacity (due to its high density) and better antibacterial properties [31]. Furthermore, Hf-containing bio-HEAs have been reported previously [24,32]. Three novel alloys were developed by adding Si, B and Ga to the TiZrNbHf equiatomic alloy. These are biocompatible elements and comply with the Inoue's empirical rules for glass formation [33], exhibiting a large atomic radii (r_i) difference and a large negative heat of mixing (H_{ij}) with the major elements Ti, Nb, Zr and Hf (Fig. 1(a)). Si was added in large proportions as a 'principal' element, while B and Ga were used as micro-alloying additions, to further "confuse" the system and increase the GFA [15,34,35]. A similar method for enhancing both the glass-forming and high-entropy effects were also applied in the (Ti, Zr, Hf)–(Ni, Cu)–Al [36] and Fe-(Ga, Al)-(P, B, Si, C) alloy systems [37]. Furthermore, in small amounts, Ga has bactericidal activity and prevents biofilm formation on the implant surface, reducing the infection risks [38]. The new developed MPEAs are: $Ti_{20}Zr_{20}Nb_{20}Hf_{20}Si_{20}$ (A1), $Ti_{30}Zr_{25}Nb_{25}Si_{15}Ga_3B_2$ (A2) and $Ti_{20}Zr_{20}Nb_{20}Hf_{20}Si_{15}Ga_3B_2$ (A3).

The compositional design strategy for high entropy alloys takes into consideration both thermodynamic and geometrical factors affecting phase formation [22]. Several semi-empirical criteria for phase selection were developed and tested using as-cast HEAs, which often contain non-equilibrium phases. [22,39,40] were the first who identified the importance of the differences of the atomic sizes (δr) and enthalpy of mixing (ΔH_{mix}) in the formation of single-phase solution solid (SS), intermetallic compounds or amorphous phases, in as-cast HEAs. These parameters were calculated using the equations from [22] and listed in Table 1. The equations are listed below:

$$\Delta H_{mix} = \sum_{i<j} 4H_{ij}c_ic_j$$

$$\delta r = \sqrt{\sum c_i(1 - r_i/\bar{r})^2}.100\%$$

where r_i and c_i are atomic radius and atomic fraction of element i; $\bar{r}$ is the average atomic radius ($\bar{r} = \sum c_i r_i$), and H_{ij} is an enthalpy of mixing of elements i and j, which values are calculated by using Miedema's model as given in [41] and presented in Fig. 1(a).

For purpose of comparison, the ΔH_{mix} and δr for some other HEAs (with biocompatible compositions) and equiatomic multicomponent metallic glasses reported in literature are listed in Table 1. For clarity, the ΔH_{mix} and δr values from Table 1 are plotted in Fig. 1(b), to show how these parameters reflecting the collective behaviour of the constituent alloying elements, can affect the phase stability in multi-principal element compositions, particularly to reveal the rules governing the formation of solid solution phases and amorphous phases.

Statistical analyses [22,39,40,47,48] of existing experimental data for HEAs produced by casting revealed that SS phases can form when δr is small ($\delta r < 6.2\%$) and ΔH_{mix} is either slightly positive or insignificantly negative (-12 kJ/mol $< \Delta H_{mix} < 5$ kJ/mol), while intermetallic phases can be present in HEAs for which $\delta r > 3\%$ and $\Delta H_{mix} < 0$ kJ/mol. In general, the ΔH_{mix} range for intermetallics partially overlaps with the ΔH_{mix} ranges for SS and amorphous phases. Almost exactly contrary to the SS requirements, the amorphous phase can form when δr is large and ΔH_{mix} is noticeably negative ($\delta r > 6.2\%$), -40 kJ/mol $< \Delta H_{mix} < -12$ kJ/mol, as marked by yellow dashed line in Fig. 1(b). According to the these criteria, the A0 (with small δ of 4.86% and ΔH_{mix} of 2.5 kJ/mol) can form a solid solution, whereas A1, A2 and A3 are not expected to form a single-phase solid solution owing to the large δ values (11.08 to 11.84%) and negative ΔH_{mix} (-28.05 to -32.8 kJ/mol). Fig. 1(b) depicts the ΔH_{mix}- δ plot indicating the positions of studied alloys. The newly developed alloys A1, A2 and A3 are within the range of forming amorphous phase proposed by Zhang et al. [40] and in general agreement with the empirical Inoue's rules [33] for glass formation. Hence, the ΔH_{mix}- δr data predict that the A1, A2 and A3 alloys can form amorphous phases, depending on the cooling rates and processing

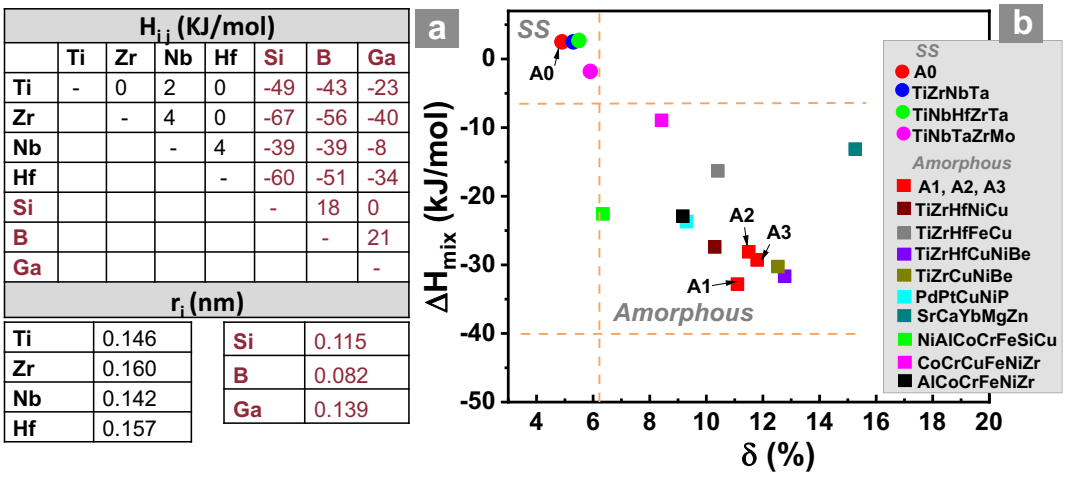

H_{ij} (KJ/mol)	Ti	Zr	Nb	Hf	Si	B	Ga
Ti	-	0	2	0	-49	-43	-23
Zr		-	4	0	-67	-56	-40
Nb			-	4	-39	-39	-8
Hf				-	-60	-51	-34
Si					-	18	0
B						-	21
Ga							-

r_i (nm)			
Ti	0.146	Si	0.115
Zr	0.160	B	0.082
Nb	0.142	Ga	0.139
Hf	0.157		

Fig. 1. (a) Mixing enthalpy ΔH_{ij} calculated by the Miedema's model for ij atomic pairs and atomic radii of the elements r_i (these data were obtained from [41]); (b) ΔH_{mix}- δ plot showing the positions of studied alloys in comparison with other MPEAs (values are taken from Table 1).

Table 1
Calculated ΔH_{mix} and δr values of the studied alloys in comparison with other equiatomic multicomponent metallic glasses and HEAs reported in literature.

Alloys	Structure	ΔH_{mix} [kJ·mol^{-1}]	δr [%]	Ref.
$Ti_{25}Zr_{25}Nb_{25}Hf_{25}$ (A0)	bcc (HEA)	2.5	4.86	Present study
$Ti_{20}Zr_{20}Nb_{20}Hf_{20}Si_{20}$ (A1)	Amorphous (ribbon)	−32.8	11.08	Present study
$Ti_{30}Zr_{25}Nb_{25}Si_{15}Ga_3B_2$ (A2)	Amorphous (ribbon)	−28.05	11.45	Present study
$Ti_{20}Zr_{20}Nb_{20}Hf_{20}Si_{15}Ga_3B_2$ (A3)	Partially amorphous (ribbon)	−29.30	11.84	Present study
$Ti_{25}Zr_{25}Nb_{25}Ta_{25}$	bcc (HEA)	2.5	5.3	[42]
$Ti_{20}Nb_{20}Hf_{20}Zr_{20}Ta_{20}$	bcc (HEA)	2.7	5.5	[43]
$Ti_{20}Nb_{20}Ta_{20}Zr_{20}Mo_{20}$	bcc (HEA)	−1.8	5.9	[44]
$Ti_{20}Zr_{20}Hf_{20}Ni_{20}Cu_{20}$	Amorphous (BMG)	−27.36	10.32	[25]
$Ti_{20}Zr_{20}Hf_{20}Fe_{20}Cu_{20}$	Amorphous (ribbon)	−16.32	10.41	[25]
$Ti_{16.7}Zr_{16.7}Hf_{16.7}Cu_{16.7}Ni_{16.7}Be_{16.7}$	Amorphous (BMG)	−31.67	12.77	[45]
$Ti_{20}Zr_{20}Cu_{20}Ni_{20}Be_{20}$	Amorphous (BMG)	−30.24	12.53	[27]
$Pd_{20}Pt_{20}Cu_{20}Ni_{20}P_{20}$	Amorphous (BMG)	−23.68	9.29	[26]
$Sr_{20}Ca_{20}Yb_{20}Mg_{20}Zn_{20}$	Amorphous (BMG)	−13.12	15.26	[28,45]
$(NiAlCoCrFeSi)_{99.5}Cu_{0.5}$	Amorphous (BMG)	−22.58	6.35	[46]
$(CoCrCuFeNi)_{99.4}Zr_{0.6}$	Amorphous (ribbon)	−8.93	8.42	[23]
$(AlCoCrFeNi)_{99.4}Zr_{0.6}$	Amorphous (ribbon)	−22.91	9.17	[23]

parameters.

The microstructure and phase formation were experimentally investigated by XRD and DSC. Fig. 2(a) shows the XRD patterns of studied alloys. The starting composition TiZrNbHf (A0) has a single-phase bcc structure typical for HEAs. The XRD patterns of $Ti_{20}Zr_{20}Nb_{20}Hf_{20}Si_{20}$ (A1) and $Ti_{30}Zr_{25}Nb_{25}Si_{15}Ga_3B_2$ (A2) detect a nearly fully amorphous structure with the typical broad diffraction peaks, characteristic of a disordered structure. For the $Ti_{20}Zr_{20}Nb_{20}Hf_{20}Si_{15}Ga_3B_2$ (A3), a partially crystalline structure has been detected (bcc and $(Ti,Nb)_2(Zr,Hf)_3Si_3$ with Bragg reflections being superimposed on broad peak of the amorphous phase).

Fig. 2(b) shows the DSC curves of studied alloys. The bcc A0 alloy has not exhibited any exo-/endothermic phase transformation peaks below 1000 K. For A1, A2, A3 ribbons, a strong exothermic peak is observed confirming that a significant fraction of amorphous phase was formed by melt-spinning. An obvious endothermic event that may indicate a glass transition is not clearly detected, which is a typical behaviour for marginal glass-former compositions with reduced GFA [15]. The high crystallization onset temperatures (T_x) ranging between 888 K and 941 K indicate a much higher thermal stability than that of other Ti- and Zr-based MGs (e.g. $Ti_{60}Zr_{15}Nb_{10}Si_{15}$, T_x = 760 K [15], $Ti_{40}Zr_{10}Cu_{34}Pd_{14}Ga_2$, T_x = 713 K [49], $Zr_{48}Cu_{36}Al_8Ag_8$, T_x = 782 K [49]). The high crystallization temperatures can be explained by the reduced diffusion kinetics in complex concentrated TiZrNb(*Hf*)Si compositions originating from a more efficient atomic packing density in these alloys [50].

The melt-spun alloy microstructure significantly depends on the processing parameters, especially on the ejection temperature of the melt during melt-spinning [15]. Fig. 2(c) displays the XRD spectra of A1-TiZrNbHfSi ribbons obtained with the same peripheral wheel velocity but different overheating temperatures of the melt before casting. A nearly fully amorphous structure has been obtained even at high melt temperatures of 2193 K. At insufficient overheating, the unmelted impurities may act as nucleation seeds, resulting in part amorphous - part crystalline microstructure. This effect is more pronounced in Ga- containing compositions (A2 and A3). Despite its low melting temperature (T_m = 303 K), gallium has a very high boiling point (T_b = 2673 K) and it forms intermetallides with Ti/Zr/Nb/Hf/Si of very high stability [51]. This could be the underlying reason for A3 composition not yielding a fully amorphous structure, even at higher overheating melt temperatures of about 2200 K (maximum operation limit of our device). Compared with the conventional Ti-based BMGs, the present glassy alloys exhibit a lower GFA, which may represent a major obstacle for applications, because bulk dimensions are challenging to achieve by casting. However, this drawback could be overcome by using additive manufacturing methods, as recently reported for conventional Ti-based metallic glasses [52].

Due to the fact that corrosion is the most frequently associated

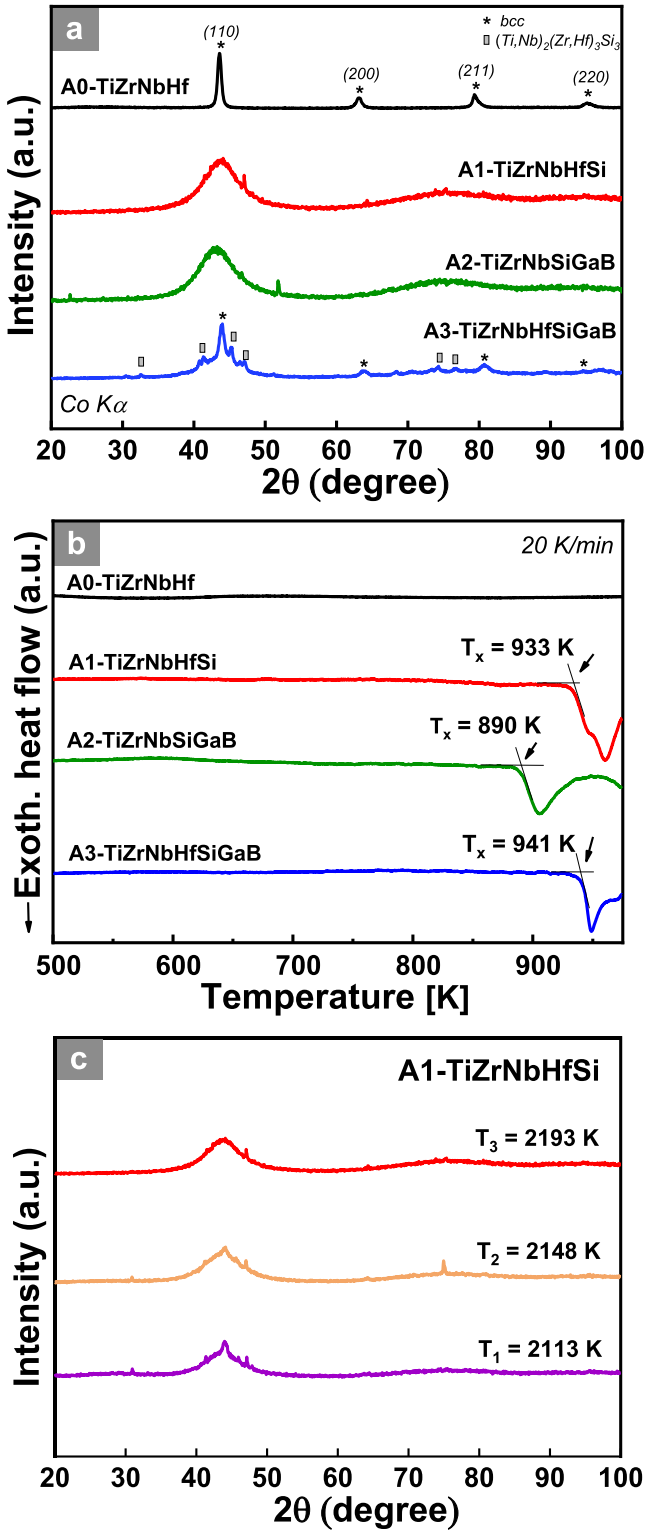

Fig. 2. (a) X-ray diffraction patterns and (b) DSC traces of the alloys (A0 –rod 3 mm ϕ, A1, A2, A3 – melt-spun ribbons); (c) dependence of amorphous nature on the overheating temperature of the melt for A1-$Ti_{20}Zr_{20}Nb_{20}Hf_{20}Si_{20}$ melt-spun alloy (tangential speed of the copper wheel was 40 m/s for all the ribbons).

degradation process leading to adverse biological reactions and implant failures, it is imperative to investigate the corrosion behaviour of the newly developed alloys [53]. Potentiodynamic polarization curves recorded for A1, A2 and A3 alloy ribbons in Ringer solution at 37 °C

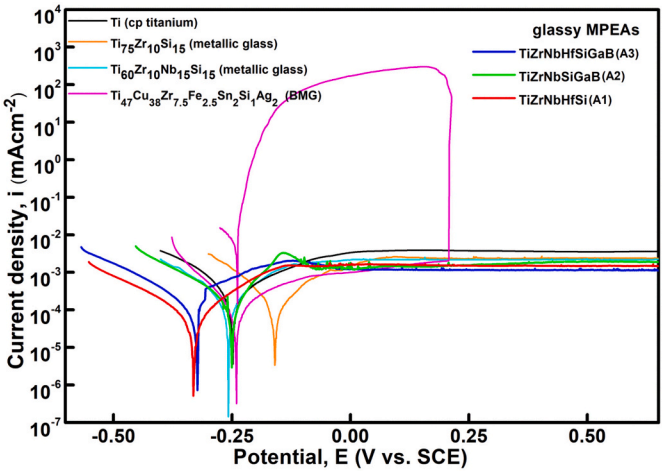

Fig. 3. Anodic polarization curves of A1, A2 and A3 MPEAs ribbons in Ringer's solution at 37 °C; the curves of other conventional metallic glasses and cp-Ti reference material are presented for comparison.

were compared with those for different reference glassy Ti-based materials developed in our group [15,18,52], measured under similar conditions. Fig. 3 shows anodic polarization curves recorded in Ringer's solution at 310 K. The corrosion potentials of those alloys are determined by their composition, their surface finishing state and the pre-immersion history [54]. Consequently, the respective sharp minima in the polarization curves do not show a composition-dependent trend, typical values are in a range from −0.15 to −0.35 V vs. SCE. Table 2 summarizes the electrochemical parameters of the A1, A2 and A3 alloys and other conventional metallic glasses, for comparison [15,18,52]. Similar to the reference materials, the new glassy MPEAs demonstrate very low corrosion current densities of ≪1 μA/cm^2 indicating very low metal ion release rates. Upon anodic polarization, a direct transition into a stable plateau of passivity occurs. Even in this concentrated body fluid, stable passivity was detected within the whole stability range of water. Passive current densities are quite low, i.e. only a few μA/cm^2, whereby for all glassy alloys slightly lower values compared to commercially pure-Ti (cp-Ti) were measured. There is no significant difference in the behaviour of the three glassy MPEAs indicating that their compositional variation has no remarkable impact. The advantage of this new alloy type is especially evident when comparing with a $Ti_{47}Cu_{38}Zr_{7.5}Fe_{2.5}Sn_2Si_1Ag_2$ bulk glass former (purple colour curve). Those Cu-containing Ti-based glasses exhibit pronounced chloride-induced pitting and limited re-passivation ability as obvious from the steep anodic current density rise and the wide hysteresis upon reverse scanning. The revealed excellent passivation ability of the new glassy alloys A1, A2 and A3 is attributable to their composition of only valve-metal components and Si yielding the growth of laterally uniform barrier-type oxide films. Earlier studies on Ti and crystalline Ti-based alloys with other valve-metal constituents in Ringer's solution comprised also

Table. 2
Electrochemical corrosion parameters obtained from potentiodynamic polarization curves determined using Tafel plot analysis.

	E_{corr} [V vs. SCE]	I_{corr} [μA/cm^2]	I_{pass} [μA/cm^2] at 0.150 V vs. SCE
cp-Ti	−0.25	0.26	3.5
$Ti_{20}Zr_{20}Nb_{20}Hf_{20}Si_{20}$ (A1)	−0.33	0.08	1.6
$Ti_{30}Zr_{25}Nb_{25}Si_{15}Ga_3B_2$ (A2)	−0.25	0.15	1.4
$Ti_{20}Zr_{20}Nb_{20}Hf_{20}Si_{15}Ga_3B_2$ (A3)	−0.32	0.13	1.1
$Ti_{75}Zr_{10}$ Si_{15}	−0.16	0.11	2.4
$Ti_{60}Zr_{10}Nb_{15}Si_{15}$	−0.257	0.17	2.2
$Ti_{47}Cu_{38}Zr_{7.5}Fe_{2.5}Sn_2Si_1Ag_2$	−0.24	0.11	1.9

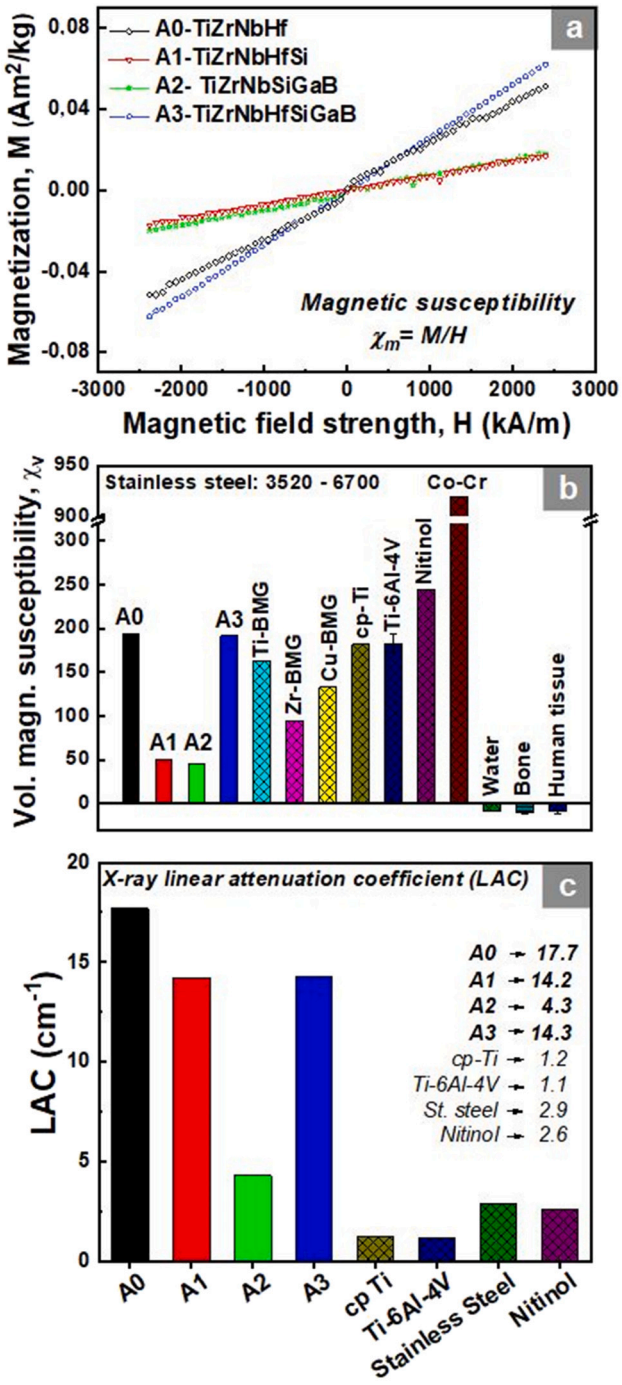

Fig. 4. (a) The magnetization vs applied magnetic field recorded for A0, A1, A2, A3; (b) volume susceptibility values of studied MPEAs presented in comparison with other alloys and human tissues [2,5,6,19]; (c) radiopacity in terms of X-ray linear attenuation coefficient (inset: LAC values for the studied materials and other commercial biomedical alloys).

electrochemical impedance spectroscopy (EIS). EIS analysis at various potentials in the passive region revealed in all cases a characteristic capacitive response which is typical for compact barrier-type passive films [55–57]. A similar behaviour is quite predictable for the glassy MPEAs, such comprehensive analysis will be the subject of next studies.

For MRI-guided surgeries or diagnostics, materials with an ultralow magnetic susceptibility are required, approaching as much as possible the values of the surrounding tissues (χ_v = −7 to −11 ppm for body tissues) [30]. Differences in magnetic susceptibilities of tissues and implanted metallic devices distort the homogeneity of the magnetic field and produce a variety of image artefacts. Moreover, interactions between the magnetic resonance environment and implants (exertion of force, voltage induction, eddy current heating) may pose severe health risks to the patient if the implant material has a high magnetic susceptibility [1]. In order to evaluate magnetic field interactions for studied materials in association with exposure to an MRI system, the magnetic susceptibility was determined by field dependent magnetization measurements (Fig. 4(a)). Magnetization variation with applied magnetic field of all four alloys (A0, A1, A2, A3) exhibited a weak paramagnetic nature advantageous for reducing the MRI artefacts. Chovan et al. emphasized the role of grain boundaries in the case of polycrystalline materials, which will act as an energy barrier to be overcome by the applied magnetic field resulting in a non-linear M(H)-dependence at low magnetic fields [58]. Therefore, the A1 and A2 alloys with an almost fully amorphous structure show a linear paramagnetic behaviour even at very low magnetic fields as compared to A3 which exhibited a partially crystalline structure. Besides the absence of crystalline defects, the lowest values of magnetic susceptibility of A1 and A2 samples can be also attributed to the increased concentration of diamagnetic alloying elements such as Si, B and Ga. In Fig. 4(b) and Table 3 the volume magnetic susceptibility values (χ_v) of studied alloys are presented and compared with clinically relevant materials (e.g. cp-Ti, Ti-6Al-4V, stainless steel, Nitinol, Co-Cr alloys) and some other alloys reported in literature as MRI compatible [2,5,6,19]. The glassy A1 and A2 alloys

Table 3
Volume susceptibility values of studied MPEAs in comparison with other alloys and human tissues.

Material	Volume magnetic susceptibility, χ_v [ppm]	Reference
$Ti_{25}Zr_{25}Nb_{25}Hf_{25}$ (A0)	193	Present study
$Ti_{20}Zr_{20}Nb_{20}Hf_{20}Si_{20}$ (A1)	50.35	Present study
$Ti_{30}Zr_{25}Nb_{25}Si_{15}Ga_3B_2$ (A2)	45.93	Present study
$Ti_{20}Zr_{20}Nb_{20}Hf_{20}Si_{15}Ga_3B_2$ (A3)	191.46	Present study
Ti-BMG	163	[19]
Zr-BMG	95	[19]
Cu-BMG	133	[19]
cp-Ti	182	[5]
Ti-6Al-4V	183	[5]
Nitinol	245	[60]
Stainless steel	3520–6700	[60]
Co-Cr alloy	920	[19]
Water	−9	[30]
Bone	−12 to −8	[30]
Human tissue	−11 to −7	[30]

Table 4
Physical properties relevant for LAC estimation [61].

Element	Atomic number	Mass attenuation coefficient [cm^2/g]	Density [g/cm^3]	X-ray linear attenuation coefficient at 100 keV [cm^{-1}]
Ti	22	0.272	4.51	1.224
Zr	40	0.965	6.49	6.263
Nb	41	1.037	8.57	8.887
Hf	72	4.154	13.07	54.411
Si	14	0.183	2.33	0.427
B	5	0.139	2.37	0.329
Ga	31	0.519	5.91	3.071
Ni	28	0.444	8.91	3.955
Al	13	0.170	2.71	0.460
V	23	0.287	6.11	1.664

exhibit ultralow magnetic susceptibility ($\chi_{v,A1}$ = 50 ppm, $\chi_{v,A2}$ = 45 ppm) less than one-third of that of commercial biomedical Ti-based materials (cp-Ti and Ti-Al-V with χ_v = 173–193 ppm [59]) and other metallic glasses (e.g. $Ti_{47}Cu_{38}Zr_{7.5}Fe_{2.5}Sn_2Si_1Ag_2$ (χ_v = 163 ppm), $Zr_{61}Ti_2Cu_{25}Al_{12}$ (χ_v = 95 ppm) or $Cu_{50.4}Ti_{31}Zr_{13}Ni_{5.6}$ (χ_v = 133 ppm) [19]). This result indicates that the glassy A1 and A2 alloys may reduce the artefacts in MRI, allowing a better soft tissue contrast compared to conventional metallic biomaterials.

Apart from MRI compatibility, the candidate materials for these miniaturized applications should also be radiopaque, in case the accurate monitoring of implant position by X-ray fluoroscopy imaging systems is required. Radiopacity is directly proportional to X-ray Linear Attenuation Coefficient (LAC), which can be calculated using the simple rule of mixtures [8].

For an alloy system with elements 1,2,…,n.

$$LAC_{alloy} = [(LAC_1 \times at\%_1) + (LAC_2 \times at\%_2) + \ldots + (LAC_n \times at\%_n)]$$

where, LAC_n denotes the linear attenuation coefficient of the n^{th} element and $at.\%_n$ represents the atomic percentage of the n^{th} element in the alloy.

LAC_n (in cm^{-1}) at 100 keV of the component elements are: 1.224^{Ti}; 6.263^{Zr}; 8.887^{Nb}; 54.41^{Hf}; 0.427^{Si}; 0.329^{B} and 3.071^{Ga} as presented in Table 4 [61]. In Fig. 4(c) are inserted the calculated LAC values of A0, A1, A2, A3 alloys and other reference materials [1].

Fig. 4(c) shows that the present alloys possess better radiopacity (higher LAC values) compared to predominant stent (stainless steel and nitinol) and aneurysm clip (Ti, Ti-6Al-4V) materials [1]. These higher attenuation coefficients exhibited by A0, A1 and A3 can be well correlated with the presence of high density element Hf.

4. Conclusions

In summary, novel biocompatible glassy Ti-Zr-Nb-Hf-Si alloys based on HEA approach was developed. The newly developed multi-principal element alloys have biocompatible compositions, with magnetic susceptibility tailored to the medical MRI environment. They exhibit high thermal stability and excellent corrosion stability in simulated body fluid. All alloys show a weak paramagnetic nature advantageous for reducing the MRI artefacts. In addition, they exhibit higher X-ray linear attenuation coefficients relevant for interventional X-ray-based medical imaging. This two-fold advantage (lower magnetic susceptibility and higher radiopacity) allows the materials to be more precisely visualized via biomedical imaging methods, which is especially important for miniaturized implants such as coronary stents or aneurysm clips.

These results provide a guideline on how to design equiatomic multicomponent metallic glasses with unique combination of biomedical properties by utilizing HEA characteristics, and thus providing a strategy for bridging MGs and HEAs fields for the discovery of new alloys of scientific significance and practical benefit.

CRediT authorship contribution statement

Mariana Calin: Conceptualization, Supervision, Writing - original draft. **Jithin Vishnu:** Formal analysis, Discussion of results and manuscript preparation, Visualization. **Pramote Thirathipviwat:** Investigation, Data curation. **Monica-Mihaela Popa:** Investigation, Data curation. **Maria Krautz:** Reviewing and editing, Validation, Data curation. **Geetha Manivasagam:** Reviewing and editing, Validation. **Annett Gebert:** Supervision, Formal analysis, Discussion of results and manuscript preparation.

Declaration of competing interest

The authors declare that they have no known competing financial interests or personal relationships that could have appeared to influence the work reported in this paper.

Acknowledgment

The authors would like to gratefully acknowledge Andrea Voß, Birgit Bartusch, Birgit Opitz and Sven Donath for valuable technical support.

Funding

M.C. acknowledges the financial support from the European Union's Horizon 2020 research and innovation programme under the Marie Skłodowska-Curie grant agreement No. 861046 (BIOREMIA).

References

[1] F.G. Shellock, J.A. Tkach, P.M. Ruggieri, T.J. Masaryk, P.A. Rasmussen, Am. J. Neuroradiol. 24 (2003) 463.
[2] G. Mani, M.D. Feldman, D. Patel, C.M. Agrawal, Biomaterials 28 (2007) 1689–1710.
[3] J. Vishnu, G. Manivasagam, Medical Devices & Sensors 3 (2020), e10116.
[4] F. Okabe, H.Y. Kim, S. Miyazaki, Scr. Mater. 162 (2019) 412–415.
[5] B.J. O'Brien, J.S. Stinson, D.A. Boismier, W.M. Carroll, Biomaterials 29 (2008) 4540–4545.
[6] H.F. Li, F.Y. Zhou, L. Li, Y.F. Zheng, Sci. Rep. 6 (2016) 24414.
[7] Y.H.R. Chang, T.L. Yoon, T.L. Lim, M.H. Tuh, Scr. Mater. 178 (2020) 82–85.
[8] B. O'Brien, J. Stinson, W. Carroll, Acta Biomater. 4 (2008) 1553–1559.
[9] A.L. Greer, Mater. Today 12 (2009) 14–22.
[10] H.F. Li, Y.F. Zheng, Acta Biomater. 36 (2016) 1–20.
[11] L. Huang, C. Pu, R.K. Fisher, D.J.H. Mountain, Y. Gao, P.K. Liaw, W. Zhang, W. He, Acta Biomater. 25 (2015) 356–368.
[12] M.D. Demetriou, A. Wiest, D.C. Hofmann, W.L. Johnson, B. Han, N. Wolfson, G. Wang, P.K. Liaw, JOM 62 (2010) 83–91.
[13] P. Rocher, L. El Medawar, J.C. Hornez, M. Traisnel, J. Breme, H.F. Hildebrand, Scr. Mater. 50 (2004) 255–260.
[14] J. Paillier, C. Mickel, P.F. Gostin, A. Gebert, Mater. Charact. 61 (2010) 1000–1008.
[15] M. Calin, A. Gebert, A.C. Ghinea, P.F. Gostin, S. Abdi, C. Mickel, J. Eckert, Mater. Sci. Eng. C 33 (2013) 875–883.
[16] M. Saito, R. Arakaki, A. Yamada, T. Tsunematsu, Y. Kudo, N. Ishimaru, Int. J. Mol. Sci. 17 (2016) 202.
[17] C.H. Lin, C.H. Huang, J.F. Chuang, J.C. Huang, J.S.C. Jang, C.H. Chen, Mater. Sci. Eng. C 33 (2013) 4520–4526.
[18] S. Abdi, S. Oswald, P.F. Gostin, A. Helth, J. Sort, M.D. Baró, M. Calin, L. Schultz, J. Eckert, A. Gebert, J Biomed Mater Res B Appl Biomater 104 (2016) 27–38.
[19] D.-B. Zhou, S.-P. Wang, S.-G. Wang, H.-J. Ai, J. Xu, J. Mater. Sci. Technol. 32 (2016) 496–504.
[20] J.A. Horton, D.E. Parsell, MRS Proc. 754 (2011), CC1.5.
[21] D.B. Miracle, O.N. Senkov, Acta Mater. 122 (2017) 448–511.
[22] O.N. Senkov, D.B. Miracle, J. Alloys Compd. 658 (2016) 603–607.
[23] S. Guo, Q. Hu, C. Ng, C.T. Liu, Intermetallics 41 (2013) 96–103.
[24] T. Nagase, Y. Iijima, A. Matsugaki, K. Ameyama, T. Nakano, Mater. Sci. Eng. C 107 (2020) 110322.
[25] L. Ma, L. Wang, T. Zhang, A. Inoue, Mater. Trans. 43 (2002) 277–280.
[26] A. Takeuchi, N. Chen, T. Wada, Y. Yokoyama, H. Kato, A. Inoue, J.W. Yeh, Intermetallics 19 (2011) 1546–1554.
[27] H.Y. Ding, K.F. Yao, J. Non-Cryst. Solids 364 (2013) 9–12.
[28] X.Q. Gao, K. Zhao, H.B. Ke, D.W. Ding, W.H. Wang, H.Y. Bai, J. Non-Cryst. Solids 357 (2011) 3557–3560.
[29] Y.D. Wu, Y.H. Cai, T. Wang, J.J. Si, J. Zhu, Y.D. Wang, X.D. Hui, Mater. Lett. 130 (2014) 277–280.
[30] J.F. Schenck, Med. Phys. 23 (1996) 815–850.
[31] F. Ostadhossein, S.K. Misra, I. Tripathi, V. Kravchuk, G. Vulugundam, D. LoBato, L. E. Selmic, D. Pan, Biomaterials 181 (2018) 252–267.
[32] A. Motallebzadeh, N.S. Peighambardoust, S. Sheikh, H. Murakami, S. Guo, D. Canadinc, Intermetallics 113 (2019) 106572.
[33] A. Inoue, Acta Mater. 48 (2000) 279–306.
[34] S. Bera, B. Sarac, S. Balakin, P. Ramasamy, M. Stoica, M. Calin, J. Eckert, Mater. Des. 120 (2017) 204–211.
[35] S. Bera, P. Ramasamy, D. Şopu, B. Sarac, J. Zálešák, C. Gammer, M. Stoica, M. Calin, J. Eckert, J. Alloys Compd. 793 (2019) 552–563.
[36] K.B. Kim, P.J. Warren, B. Cantor, Mater. Sci. Eng. A 375-377 (2004) 317–321.
[37] A. Inoue, F.L. Kong, S.L. Zhu, A.L. Greer, MRS Bull. 44 (2019) 867–872.
[38] Y. Kaneko, M. Thoendel, O. Olakanmi, B.E. Britigan, P.K. Singh, J. Clin. Invest. 117 (2007) 877–888.
[39] S. Guo, C.T. Liu, Progress in Natural Science: Materials International 21 (2011) 433–446.
[40] Y. Zhang, Y.J. Zhou, J.P. Lin, G.L. Chen, P.K. Liaw, Adv. Eng. Mater. 10 (2008) 534–538.
[41] A. Takeuchi, A. Inoue, Mater. Trans. 46 (2005) 2817–2829.
[42] M. Todai, T. Nagase, T. Hori, A. Matsugaki, A. Sekita, T. Nakano, Scr. Mater. 129 (2017) 65–68.
[43] O.N. Senkov, J.M. Scott, S.V. Senkova, D.B. Miracle, C.F. Woodward, J. Alloys Compd. 509 (2011) 6043–6048.

[44] S.-P. Wang, J. Xu, Mater. Sci. Eng. C 73 (2017) 80–89.
[45] H.Y. Ding, Y. Shao, P. Gong, J.F. Li, K.F. Yao, Mater. Lett. 125 (2014) 151–153.
[46] Y.Y. Chen, T. Duval, U.T. Hong, J.W. Yeh, H.C. Shih, L.H. Wang, J.C. Oung, Mater. Lett. 61 (2007) 2692–2696.
[47] W.H. Wang, JOM 66 (2014) 2067–2077.
[48] Y. Zhang, S. Guo, C.T. Liu, X. Yang, Phase formation rules, in: M.C. Gao, J.-W. Yeh, P.K. Liaw, Y. Zhang (Eds.), High-entropy Alloys: Fundamentals and Applications, Springer International Publishing, Cham, 2016, pp. 21–49.
[49] B. Sarac, S. Bera, F. Spieckermann, S. Balakin, M. Stoica, M. Calin, J. Eckert, Scr. Mater. 137 (2017) 127–131.
[50] M.-H. Tsai, C.-W. Wang, C.-W. Tsai, W.-J. Shen, J.-W. Yeh, J.-Y. Gan, W.-W. Wu, J. Electrochem. Soc. 158 (2011) H1161.
[51] A. Cochis, B. Azzimonti, R. Chiesa, L. Rimondini, M. Gasik, ACS Biomaterials Science & Engineering 5 (2019) 2815–2820.
[52] L. Deng, S. Wang, P. Wang, U. Kühn, S. Pauly, Mater. Lett. 212 (2018) 346–349.
[53] M. Geetha, A.K. Singh, R. Asokamani, A.K. Gogia, Prog. Mater. Sci. 54 (2009) 397–425.
[54] A. Gebert, P.F. Gostin, L. Schultz, Corros. Sci. 52 (2010) 1711–1720.
[55] J.E.G. González, J.C. Mirza-Rosca, J. Electroanal. Chem. 471 (1999) 109–115.
[56] C. Vasilescu, S.I. Drob, P. Osiceanu, J.M.C. Moreno, M. Prodana, D. Ionita, I. Demetrescu, M. Marcu, I.A. Popovici, E. Vasilescu, Metall. Mater. Trans. A 48 (2017) 513–523.
[57] M.T. Woldemedhin, D. Raabe, A.W. Hassel, Electrochim. Acta 82 (2012) 324–332.
[58] D. Chovan, A. Gandhi, J. Butler, S.A.M. Tofail, J. Magn. Magn. Mater. 452 (2018) 451–457.
[59] O. Beuf, M. Lissac, Y. Crémillieux, A. Briguet, Dent. Mater. 10 (1994) 265–268.
[60] B. O'Brien, J. Stinson, W. Carroll, J. Mech. Behav. Biomed. Mater. 1 (2008) 303–312.
[61] J.H. Hubbell, S.M. Seltzer, Tables of X-ray Mass Attenuation Coefficients and Mass Energy-absorption Coefficients (Version 1.4), NISTIR, National Institute of Standards and Technology, Gaithersburg, MD, 2004.